Terahertz Beam Steering With Doped GaAs Phase Modulator and a Design of Spatial-Resolved High-Speed Terahertz Analog-to-Digital Converter

Zhao Xu and Pinaki Mazumder, *Fellow, IEEE*

***Abstract*— In this paper, we have designed and characterized the beam steering structure for terahertz radiation based on doubly corrugated spoofed surface plasmon polariton (DC-SSPP) architecture and analyzed the design of a high-speed terahertz analog-to-digital converter (ADC). Two DC-SSPP waveguides comprising metal-covered GaAs are utilized to build an interferometric structure with localized doping in the groove region. Active modulation of free carrier density in the doped n-GaAs will cause relative phase differences between terahertz beams in separate arms of the interferometer, giving rise to deflected radiation in the far field. In this paper, both mathematical modeling and finite-element simulations are used to verify and optimize the design. Two different architectures operating on the enhancement mode and depletion mode are studied separately in detail. Applying the beam bender in the ADC design poses challenges such as structural symmetry and multibit resolution. With a full differential implementation of the input signal and combination of nonlinear detector arrays with carefully designed gain and saturation power, a 3-bit ADC is demonstrated with higher than 60 GS/s speed and direct digitized readout.**

***Index Terms*— Analog-to-digital converter (ADC), beam steering, doubly corrugated spoofed surface plasmon polariton (DC-SSPP), free carrier concentration, terahertz.**

I. INTRODUCTION

STRUCTURES and devices designed to work in the frequency range of 0.1–10 THz are proved to be essential in imaging, spectroscopy, biosensing, and other applications alike [1]–[4]. They are also strong candidates for building the next-generation integrated circuits that will eventually close the gap between electronics and optics [5]–[8]. Concentration of terahertz radiation in small volumes can facilitate the subwavelength transmission of the signal, generating new possibilities for low-loss, low-dispersion delivery of terahertz radiation over distance. The strong confinement of the E-M field can also enhance the signal-matter interaction, hence maximizing the modulation efficiency in active device designs [9]–[11].

Strong mode localization at terahertz frequency is realized by adding periodic surface features onto the material interface of conventional waveguide structures [12]–[15]. Unlike using resonant structures with dimensions comparable with the wavelength, the metamaterial created by the subwavelength surface modifications can support a special surface mode, named spoofed surface plasmon polariton (SSPP) mode [16]–[18]. With discrete transmission peaks and valleys, the SSPP modes can be modulated by changing geometric dimensions and material parameters of the structure. In most of the studies employing SSPP terahertz architectures, the discrete passing bands and their amplitude modulation due to external stimuli serve as the backbone of the device functionality [8], [19]–[21].

Kramers–Kronig relationship dictates coupled evolution of the real and imaginary parts of the dielectric constant. Therefore, the change in transmittance must be accompanied with the shift in phase accumulation. The inclusion of phase information is, hence, critical in the effort to achieve higher resolution and sensitivity for the SSPP terahertz devices. A metamaterial terahertz phase modulator based on metallic split-ring resonator design was proposed in [19], [22]. In their design, voltage across the Schottky contact formed by the doped semiconductor (GaAs) layer and metal electrode causes depletion of free carriers, changing the complex transmittance of the structure at terahertz frequencies. Phase modulators in the form of waveguides have also been proposed and fabricated by a number of research groups, where doped Si is used to form a thin strip ring resonator [23]–[25]. The phase of the propagating signal can be adjusted by free carrier injection through a p-i-n junction, and as a result, the coupling efficiency of the ring resonator can be modulated. Due to the large loss tangent of Si in terahertz domain however, such design can only be effectively applied up to near-infrared frequencies.

In this paper, we introduce 1-D periodic grooves on opposing interfaces of the metal–dielectric–metal waveguide to form the doubly corrugated SSPP (DC-SSPP) structure. We have demonstrated that such structure has discrete transmission bands, strong surface charge interaction, and localized energy distributions at resonance [18]. In [7] and [8], we have proposed filters and active switches using DC-SSPP structure based on its transmittance selectivity. Moreover, by combining two DC-SSPP waveguides into a Mach–Zehnder interferometer (MZI), we can extract the phase information of the propagating terahertz signal and as a result, have transmission peaks with enhanced quality factor and much

---

Manuscript received May 22, 2013; revised March 31, 2014; accepted April 14, 2014. Date of publication May 6, 2014; date of current version May 16, 2014. This work was supported by the Air Force Office of Scientific Research under Grant FA9550-12-1-0402. The review of this paper was arranged by Editor M. Thumm.

The authors are with the Department of Electrical Engineering and Computer Science, University of Michigan, MI 48109 USA (e-mail: xuzhao@umich.edu; pinakimazum@gmail.com).

Color versions of one or more of the figures in this paper are available online at http://ieeexplore.ieee.org.

Digital Object Identifier 10.1109/TED.2014.2318278

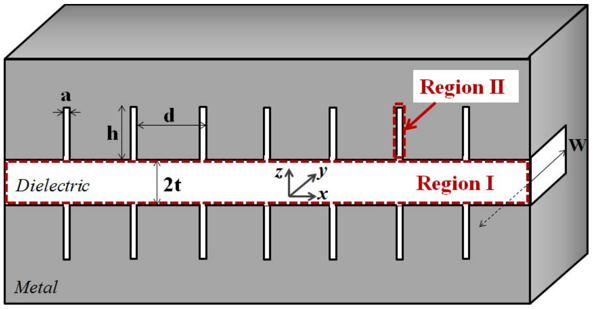

Fig. 1. Cross section of the DC-SSPP structure with different geometric dimensions labeled. W is the width of the waveguide along the y-axis. The structure can be divided into Region I and Region II as shown in the sketch.

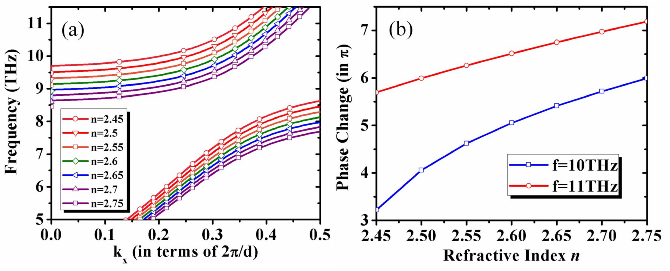

Fig. 2. (a) Dispersion relations of the DC-SSPP waveguide with changing refractive index. (b) Phase change of the terahertz wave after propagating through seven grooves. Both frequencies selected are slightly above the SSPP resonance.

higher sensitivity to external modulations. We have designed DNA biosensors based on the MZI design, and demonstrated significant enhancement to the On/Off extinction ratio in the differentiation of denatured and hybridized DNA molecules [26].

In this paper, we present a terahertz beam bender that can be actively controlled through free carrier density modulations. Based on this phenomenon, we can realize a multibit analog-to-digital converter (ADC) that utilizes terahertz signals. The paper is organized as follows. In Section II, the mathematical analysis of the DC-SSPP structure will be briefly described and phase modulation with refractive index change in a simplified model will be presented. In Sections III and IV, finite-element simulations for the terahertz beam bender operating in the enhancement mode and depletion mode are carried out, respectively, and the results are discussed. Section V will be dedicated to the design and analysis of the ADC, followed by a brief conclusion in Section VI.

II. THEORETICAL ANALYSIS

The DC-SSPP structure in this paper is sketched in Fig. 1. In order to derive the mathematical form of the dispersion relation, the whole structure is divided into two separate regions. Vector E-M fields are expressed in both regions and are connected using boundary conditions. Following a strict mathematical deduction, the mode dispersion relationship is obtained as follows:

$$1+\sum_{n=-\infty}^{\infty}\frac{k_{z,II}}{k_{z,I}^{(n)}}\frac{|T_n|^2}{\tan\left(k_{z,I}^{(n)}t\right)}\tan\left(k_{z,II}h\right)=0 \tag{1}$$

for symmetric mode, and

$$1-\sum_{n=-\infty}^{\infty}\frac{k_{z,II}}{k_{z,I}^{(n)}}|T_n|^2\tan\left(k_{z,I}^{(n)}t\right)\tan\left(k_{z,II}h\right)=0 \tag{2}$$

for antisymmetric mode, where

$$|T_n|^2=\left|\sqrt{\frac{1}{ad}}\int_0^a e^{jk_{x,I}^{(n)}x}dx\right|^2=\frac{a}{d}\left|\mathrm{sinc}\left(\frac{k_{x,I}^{(n)}}{2}a\right)\right|^2. \tag{3}$$

In the above descriptions, the symmetry of the mode is determined by the y-component of the magnetic field. Physical parameters, namely, a, d, h, t, are different geometrical dimensions of the structure as shown in Fig. 1. $k_{x,I}^{(n)}$ and $k_{z,I}^{(n)}$ denote the wavevectors of the nth-order Floquet mode along x- and z-axes in Region I, and correspondingly, $k_{x,II}$ and $k_{z,II}$ denote the wavevectors along the two axes in Region II. For a complete description of variables in the above equations and a comprehensive deduction of the dispersion relation, refer to [18].

The wavevectors as solved by (1) and (2) are functions of the refractive index n. As a result, when n is modulated by certain external stimuli, the wavevector will be altered correspondingly. Fig. 2 shows the dispersion relation of a DC-SSPP waveguide with dimensions $d = 5.1$ μm, $a/d = 0.1$, $h/d = 0.7$, $t/d = 0.3$, and $W/d = 3$, as numerically calculated using MATLAB [27]. The refractive index is set to change from 2.45 to 2.75 and is applied to the entire dielectric part of the waveguide. While the homogeneous change of the refractive index across the structure is a simplified assumption, this theoretical formulation is intrinsically fast to calculate. In this paper, it serves as the initial step in the design process before any numerical simulations are carried out.

In Fig. 2, a significant shift of the overall phase accumulation can be observed for the two frequencies chosen, which, when applied to a MZI structure, will give rise to changing interferometric output. In the design of terahertz beam bender, we apply this MZI architecture to achieve deflected beam radiation in the far field. To realize active external control, doped semiconductor is chosen as the dielectric material, and modulation to the refractive index is induced by injecting or depleting the free carriers within the semiconductor layer.

The working modes based on injection and depletion of free carriers in doped semiconductor are known as the enhancement mode and the depletion mode, respectively. We borrow these terminologies and will use them to refer to two different types of terahertz beam bender designs in the following sections. As the mathematical model can only predict phase modulation of simple architectures with accuracy, we perform the finite-element simulations on the realistic beam bender structures in order to verify the idea and optimize the design.

III. SIMULATION RESULT: ENHANCEMENT MODE

The dielectric constant of semiconductor as a function of frequency follows the Drude model. As a result of optical phonon vibrations of the crystal lattice in heteropolar semiconductors, the Drude model needs to be modified for these

TABLE I

LIST OF VARIABLES IN THE DIELECTRIC CONSTANT MODEL FOR HETEROPOLAR SEMICONDUCTORS (MODIFIED DRUDE MODEL)

ε_∞	High frequency dielectric constant
ε_s	Static dielectric constant
ε_0	Dielectric constant of vacuum
ω_p	Plasmonic resonance frequency
ω_{TO}	Transverse optical phonon resonance
ω	Frequency
Γ	Coherent decay factor of free carriers
γ	Phonon damping constant
N	Free carrier concentration
e	Charge of electron
m^*	Effective mass of electron

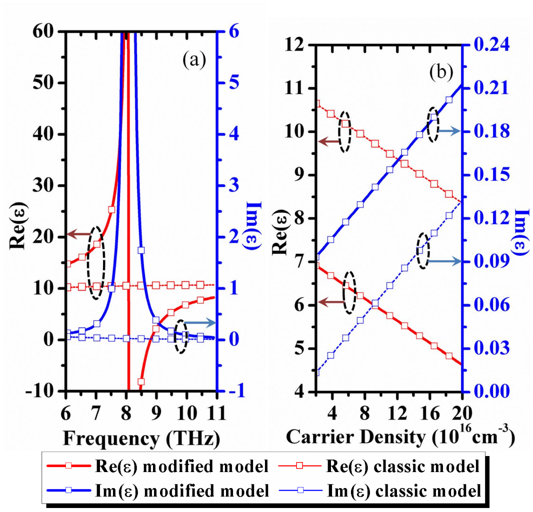

Fig. 3. Complex dielectric constant of GaAs (a) as a function of frequency at $N = 2 \times 10^{16}$ cm^{-3} and (b) as a function of free carrier density at $f = 10$ THz. Sharp peak in (a): optical phonon resonance.

materials in terahertz frequencies and is expressed as [28]

$$\varepsilon(\omega) = \varepsilon_\infty + \frac{\omega_{TO}^2(\varepsilon_s - \varepsilon_\infty)}{\omega_{TO}^2 - \omega^2 - i\omega\gamma} - \frac{\omega_p^2}{\omega(\omega + i\Gamma)} \tag{4}$$

where

$$\omega_p = \sqrt{\frac{Ne^2}{\varepsilon_0 m^*}}. \tag{5}$$

The variables in (4) and (5) are summarized in Table I. The second term in (4) represents the contribution of optical phonons, whereas the third term counts for the effect of plasmonic oscillation and coherent decay of carrier electrons. Through ω_p relationship in (5), the dielectric constant is dependent on the free carrier density N of the semiconductor.

As an example, we calculated the dielectric constant of GaAs as a function of frequency and free carrier density using (4), and the result is illustrated in Fig. 3 [29]. With the free carrier concentration of $N = 2 \times 10^{16}$ cm^{-3}, the phonon resonance can be clearly marked by the sharp peak in the curve of imaginary ε versus frequency (and abrupt change in the curve of real ε) to be 8.05 THz. To illustrate the significance of the phonon resonance, the dielectric constant calculated without the second term in (4) is also included in Fig. 3 (thin dashed line) with visibly large discrepancies.

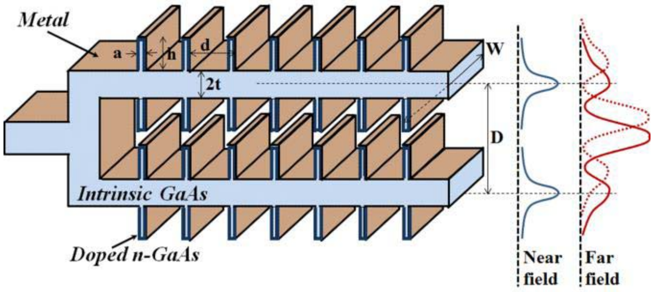

Fig. 4. Cross section of the DC-SSPP beam steering structure with different geometric dimensions labeled. W is the width of the waveguide along the y-axis. The near-field and far-field radiation patterns are qualitatively sketched.

Among the common semiconductor materials, GaAs has low intrinsic free carrier density, moderate carrier mobility, and electron effective mass. As observed from Fig. 3(b), in terahertz frequencies, GaAs demonstrates effective change of the real ε with different free carrier densities, and mild change to the small imaginary ε at the same time. Such properties are desirable in our application, where large modulation depth and stable power output throughout the working range are required. As a result, we deploy GaAs as the semiconductor material in our design of the terahertz beam bender.

The structure of the beam bender is illustrated in Fig. 4. Two arms of the DC-SSPP waveguide, each with seven grooves, are combined in the form of an MZI with separate output ports. The free propagation region follows the interferometer to let the beam travel to the far field. The entire structure is made of intrinsic GaAs covered by metal, with the only exception in the grooves, where dopants are introduced to create a thin layer of n-type GaAs. Although not a focus of this particular report, this structure can be fabricated following conventional procedures, including electron beam lithography for patterning, dopant implantation for defining the n-GaAs region, and physical vapor deposition for forming the metal shell.

The SSPP mode is largely confined to the groove region near resonance. The localized n-GaAs can, therefore, effectively lower the insertion loss of the device without sacrificing the performance. In the proposed ADC implementation, free carriers are injected into the n-GaAs layer of one or both arms via external stimuli. Such an injection can be electrical, optical, or thermal depending on its specific applications.

We use HFSS to simulate the structure as mentioned previously, with the dimensions of each SSPP arm being $d = 4.9$ μm, $a/d = 0.1$, $h/d = 0.7$, $t/d = 0.3$, $W/d = 3$, and the separation between the arms being $D/d = 2.5$ [30]. The angular output radiation from the MZI modulated by the free carrier concentration is illustrated in Fig. 5. The GaAs in this case has an initial doping concentration of $N = 2\times10^{16}$ cm^{-3}. At the operating frequency of 10 THz, such carrier density corresponds to the dielectric constant of $\varepsilon = 6.91+i0.09$ ($n = 2.63+i0.02$). In our simulation, the free carrier concentration of the n-GaAs layer of thickness $\delta = 100$ nm is changed in one arm from $N = 2 \times 10^{16}$ cm^{-3} to $N = 2 \times 10^{17}$ cm^{-3} as a result of carrier injection. Fig. 5(a) shows the change of the angular radiation power density. Accordingly, the angle

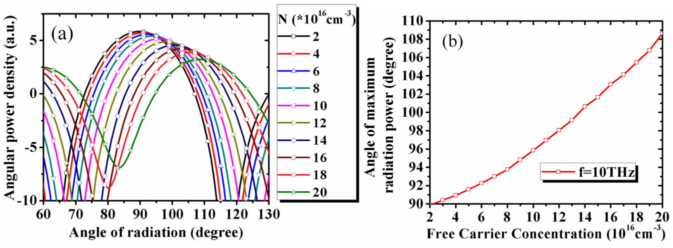

Fig. 5. (a) Angular power density of the beam bender output at $f = 10$ THz with different free carrier concentrations. (b) Angle of maximum radiation power as a function of free carrier density. 90° represents normal output.

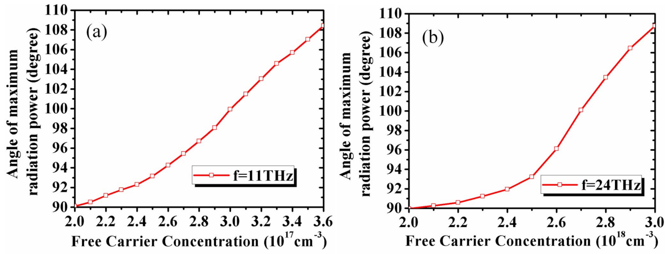

Fig. 6. Angle of maximum radiation power as a function of free carrier concentration for operation at (a) $f = 11$ THz and (b) $f = 24$ THz with adjusted structure dimensions. 90° represents the case of normal output.

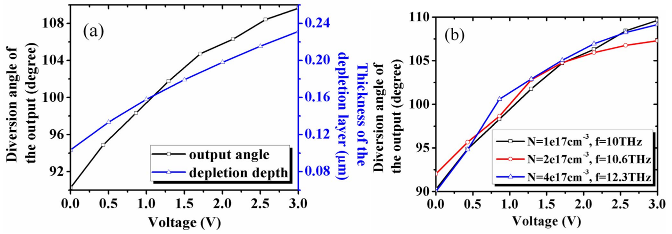

Fig. 7. (a) Thickness of the depletion layer in n-GaAs (blue) and deflection angle of the beam output (black) as a function of voltage with initial doping concentration of $N = 1 \times 10^{17}$ cm^{-3}. (b) Deflection angle of the beam output as a function of voltage for initial doping concentrations of $N = 1 \times 10^{17}$ cm^{-3}, 2×10^{17} cm^{-3}, and 4×10^{17} cm^{-3}.

of maximum power of radiation as a function of the carrier density is plotted in Fig. 5(b). A change up to 18° in the angle of radiation is observed for the MZI output.

The slight nonlinearity of the curve in Fig. 5(b) comes from the modified Drude model. From (4), (5), and Fig. 3, it is easy to notice the linear evolution of ε with N. The phase change, on the other hand, is proportional to $n = \sqrt{\varepsilon} \propto \sqrt{N}$. A simple mathematic routine of Taylor expansion, however, shows that such nonlinearity can be mostly corrected when carriers are injected in both arms in a differential manner. The insertion loss, on the other hand, is obtained as the portion of output power versus input to be 4 dB. About 2 dB of this loss is found to come from reflection of the bifurcated MZI structure and the Fabry–Perot (F-P) echelon effect, which can be further alleviated by optimizing the design therein.

In addition to the given example, the beam bending effect is not confined by specific structural dimensions. In fact, the initial doping concentration of n-GaAs and operating frequency of the structure can change in pairs, as long as the imaginary refractive index is not too large to prevent effective wave propagation. Correspondingly, the dimensions of the structure can be adjusted in scale, making this design highly adaptable to various requirements. As an example, using (4), we calculate the operating frequencies of initial doping density of $N = 2 \times 10^{17}$ cm^{-3} and $N = 2 \times 10^{18}$ cm^{-3} to be 11 and 24 THz, corresponding to the refractive indices of $n = 2.54 + i0.03$ and $n = 2.49 + i0.02$, respectively. For these operating frequencies, the beam bender has the size of $d = 4.2$ μm and $d = 1.9$ μm individually. The output angle as a function of free carrier density in those two cases is illustrated in Fig. 6. Similarly, the beam deflection is accompanied with nonlinearity, which can be effectively overcome when differential carrier injection is applied. The refractive indices in these two cases are chosen such that the insertion losses are comparable, and of which a significant contribution still comes from the MZI structure itself.

IV. SIMULATION RESULT: DEPLETION MODE

Since the doping concentration of GaAs layer is much higher than its intrinsic free carrier density ($N_i = 2.1 \times 10^6$ cm^{-3}), the terahertz beam bender can also operate in depletion mode. In this mode, a Schottky contact is formed by the metal electrode and GaAs layer. When applying voltage across the contact, the free carriers will be extracted and a depletion zone will be formed. The thickness of the depletion zone as a function of the external voltage is given by [31]

$$D_{\text{dep}} = \sqrt{\frac{2\varepsilon_s \varepsilon_0 (V_{bi} + V)}{eN}}. \tag{6}$$

Descriptions of the variables in (6) are included in Table I. $V_{\text{bi}} = 0.75$ V is the built-in voltage for the metal-GaAs junction, and V is the applied voltage [32]. The relationship of (6) is plotted in Fig. 7(a) for the doping concentration $N = 1 \times 10^{17}$ cm^{-3} in GaAs and V from 0 to 3 V.

In our design, similar MZI structure is used as in Section III, with the only exception of the n-type GaAs, which in this case occupies the entire groove region. In the depletion mode, when the n-GaAs in one arm is depleted by various thicknesses via external voltage, the phase of the propagating terahertz signal is changed and the output radiation is deflected accordingly. Such deflection effect is also illustrated in Fig. 7(a) for the structure with dimensions $d = 4.75$ μm, $a/d = 0.1$, $h/d = 0.7$, $t/d = 0.3$, $W/d = 3$, $D/d = 2.5$, and the initial free carrier concentration of $N = 1 \times 10^{17}$ cm^{-3}. The operating frequency of the structure in this case is 10 THz, and a maximum deflection angle of 19° is achieved with the voltage of 3 V. The insertion loss in this case is obtained as 7.7 dB in the worst case scenario ($V = 0$ V with minimum depletion), of which ∼4 dB results from the reflection off the bifurcated MZI structure and the F-P echelon effect. The higher loss compared with the enhancement mode also partially comes from the doped GaAs layers, which are effectively 2.5 times thicker in this case.

Similar to the enhancement mode, the beam bender in the depletion mode can operate with different combinations of frequency and doping concentrations. In Fig. 7(b), the output angle as a function of the control voltage for different initial doping concentrations up to $N = 4 \times 10^{17}$ cm^{-3} are shown and compared. The dimension of the structure is adjusted to $d = 4.4$ μm and $d = 3.7$ μm for the cases of $N = 2 \times 10^{17}$ cm^{-3} and $N = 4 \times 10^{17}$ cm^{-3}, respectively, and the operating frequencies are chosen such that effective beam deflection and comparable insertion loss are obtained. In all circumstances, the nonlinear increase of the deflection angle is caused by the proportionality between D_{dep} and $\sqrt{V_{\text{bi}} + V}$. Again, such nonlinearity can be mostly corrected when differential voltage is applied to both arms of the MZI structure.

V. DESIGN OF THE HIGH-SPEED TERAHERTZ ADC

In previous sections, we have demonstrated the beam bending effect of the DC-SSPP architecture. The ability to control the deflection angle of the output through external stimuli makes such a structure valuable in building a number of active devices. A spatial-resolved terahertz ADC is one of the many important applications.

Analog-to-digital conversion is an indispensable technology for mixed-signal circuits. Although electronic ADCs have been primarily used for the task, alternatives such as optically assisted and all-optical ADCs have been intensely studied to overcome the performance limitations of the electronic ADCs. Among them, the idea of an optical ADC operating on diverted far-field radiation patterns has been proposed in [33], where multiple phase shifters with geometrically increasing lengths were used. In recent years, further works have been conducted in an effort to realize high-speed analog-to-digital conversion. Jarrahi *et al.*, for example, have used the quantum-confined Stark effect to induce the phase change in one or both arms of an MZI waveguide consisting of travelling-wave phase shifters. The diverted beam is received by detector arrays arranged in binary manner, and digitized output is readout directly [34].

Despite its wide bandwidth (BW) in theory, the speed advantage of optical ADC has yet been fully utilized due to the lack of resonant conversion between photons and electrons. Terahertz frequency band, on the other hand, can interact coherently with electronics, and is hence a more promising candidate for building high-speed integrated components. A terahertz ADC design can serve as a gateway to emerging landscapes of broadband, terahertz-assisted, as well as all-terahertz systems.

In the terahertz domain, the index-guiding waveguide design shows small modal confinement factor and high signal power loss, hence is incapable of delivering signals at these frequencies with good beam quality and radiation efficiency. To overcome this problem, we apply the DC-SSPP structure to realize confined propagation of terahertz wave in the form of a spoofed surface mode. Room-temperature, spatial-resolved ADC operations employing terahertz carrier signals can be realized by having the DC-SSPP beam bender as the first stage, as is shown in the architecture drawing in Fig. 8.

In our design, depletion mode is chosen as the operating mode to enable beam steering, and the control voltage serves as the analog input. The change in the position of radiation maxima can be interpreted into binary bits by the detector arrays when their positions and properties are carefully designed.

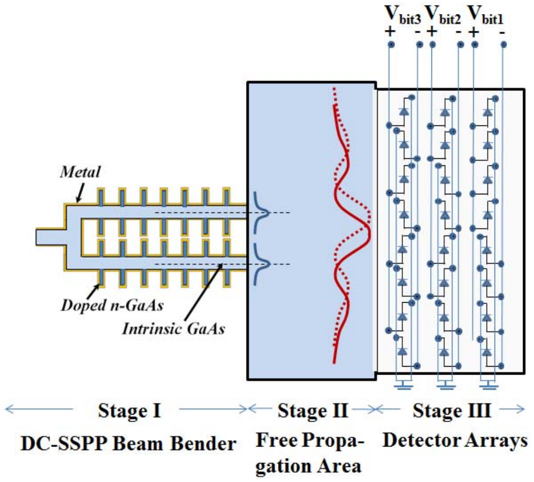

Fig. 8. Sketch of the ADC based on the DC-SSPP beam bender as the first stage.

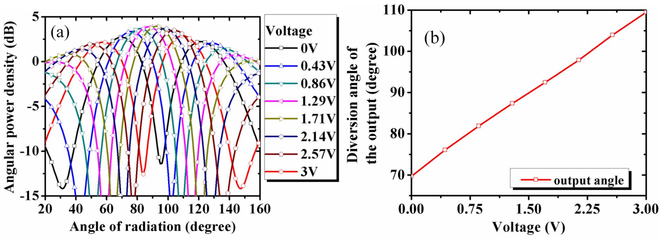

Fig. 9. (a) Angular radiation power density. (b) Deflection angle of the beam output as a function of voltage. The peak position of the radiation changes from 70° to 110° with a voltage input of 0–3 V.

A. Design of the Beam Deflector

The beam deflector stage of the terahertz ADC consists of 10 periods of grooves on each arm of the MZI structure and has dimensions of $d = 4.75$ μm, $a/d = 0.1$, $h/d = 0.7$, $t/d = 0.3$, $W/d = 3$, and $D/d = 2.5$. The initial doping concentration of the n-GaAs in the groove region is $N = 1 \times 10^{17}$ cm^{-3}. When compared with the structure in Section IV, a fully differential implementation is adopted here, where voltages are simultaneously applied to both arms of the MZI. This has resulted in a significant increase in the maximum deflection angle of the output. As shown in Fig. 9, with a voltage change of 0–3 V, the deflection angle of the terahertz output can change in a wide range of ±20°. The symmetric shift of the beam peak position over normal radiation (90°) is important in ADC operations since the detector arrays are arranged in a mirror symmetric manner. From Fig. 9(b), this symmetry along with the perfect linearity of the output angle as a function of input voltage is observed with the application of differential voltages to both arms. The insertion loss in this case is obtained as 7.9 dB. Similarly, it is expected to be significantly lowered with an improved design of the MZI structure.

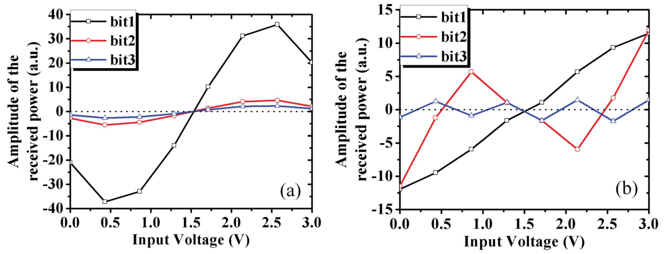

Fig. 10. 3-bit readout from the ADC with 0–3 V voltage input. (a) Linear detector arrays. (b) Nonlinear detector arrays.

TABLE II
DESIGN OF DETECTOR ARRAYS IN A 3-BIT ADC IN TERMS OF GAIN AND SATURATION POWER

Detector #	Gain (relative)	Saturation power (a.u.)
1,8	2 ×	3
2,7	2 ×	5
3,6	2 ×	7
4,5	3 ×	9

B. Design of the Detector Arrays

In ideal cases of the ADC design employing beam steering mechanisms, the main peak of the radiation pattern needs to be coupled independently into separate detectors in order to directly readout the digitized bits of the analog input. By applying classic diffraction theories, it is easy to conclude that in this case, at least $N_s = 2^n$ phase shifters in the first stage are needed in order to realize an n-bit ADC. In our design, however, only two SSPP branches are used to form the MZI structure. Therefore, for any attempt to have more than 1-bit digitized output, the radiation peak can only be partially coupled into separate detectors. The outcome as a result of the partial coupling is shown in Fig. 10(a), where eight identical linear detectors are used in an attempt to obtain a 3-bit output. It is observed that only one period of the sign change can be obtained for all 3 bits in this case, which indicates an actual ADC resolution of only 1 bit.

To tackle this problem, we need to employ detectors operating in saturated conditions. With carefully designed gains and nonlinearities for the detector arrays, we can manage to have up to 2^n periods of sign change within 2π phase shift for the nth bit output. In Table II, we have summarized an example of such a design for an array of eight detectors (#1–#8 from the top to the bottom as shown in Fig. 8). The nonunity relative gain is used to emphasize the edges of the main radiation peak. The saturation power is determined in a way that a considerable width centered on the peak position is deemed as equal by the detectors, and its value is given in the arbitrary unit so that it can be in reality proportionally adjusted to fit different terahertz source and detector specifications. Fig. 10(b) shows the digitized readout from such detector array. A 3-bit output can be obtained in this case with the analog input voltage changing from 0 to 3 V. It should be noted that in the actual realization of the ADC, the detector arrays will have finite width along the transverse dimension (y-axis) of the output beam. Due to the nonuniform power distribution along this direction, the gains and nonlinearities of the detector stages need to be adjusted accordingly.

C. BW Calculation

The effort to increase the operating BW of electrical sampling ADC is challenged by the relatively large temporal jitter of the sampling signal [35]. Recent developments in optical ADC have attempted to solve this problem using ultrastable sampling pulses of mode-locked lasers, whereas the speed of operation of such design is still limited by the BW of the E-O modulator stage. Despite the small jitter of the pulses, the repetition rate of the state-of-the-art mode-locked laser is mostly in the subgigahertz range. As a result, to date, the BW characterization of optical sampling ADCs is carried out by either using sinusoidal continuous wave analog input, or by generating significantly aliased signals after digitization with serious under-sampling [34], [36].

In our terahertz ADC design, it is helpful to calculate the operating BW of the beam deflector stage (analogy to the E-O modulator stage in optical ADC), which will give us a good idea of the speed performance of our design in comparison with its optical counterparts. In depletion mode, the Schottky contact formed by the electrode and doped GaAs layer contributes to a finite phase settling time of the modulator, which in turn will determine the operating BW of the stage as described by the following formula [34]:

$$\mathrm{BW} \le \frac{1}{2\ln 2(b+1)T_{\mathrm{set}}}. \tag{7}$$

In the above equations, T_{set} stands for the phase settling time, and b is the bit depth of the ADC ($b = 3$, in our case). T_{set} is determined by the carrier transit time and the parasitic RC time constant of the Schottky contact, which will be calculated separately in the following paragraphs.

When the space-charge region is reasonably thin, and the electric field is not very strong, the carrier transit time of a Schottky contact can be calculated mathematically. When the two terminals are separated by a distance comparable with the mean free path of the carrier motion, the electrons undergo ballistic transport, which is best described as the accelerated motion under the external bias voltage. The dc-transit time in this case can be obtained as [37]

$$\tau_{\mathrm{trans}} = \frac{\pi}{2}\sqrt{\frac{m^*\varepsilon_s\varepsilon_0}{Ne^2}} = \frac{\pi\sqrt{\varepsilon_s}}{2\omega_p}. \tag{8}$$

In our case, with $N = 1 \times 10^{17}$ cm^{-3}, τ_{trans} is calculated by (8) to be 0.08 ps. It corresponds to an average carrier drift velocity in the order of 10^6 m/s, which far exceeds the saturation drift velocity $\upsilon_{\mathrm{sat}} = 8 \times 10^4$ m/s for GaAs at this electric field intensity. This indicates that the electron motion in our case cannot be simplified as ideal ballistic transport. Instead, collision plays an important role in the carrier motion and can significantly slow it down.

The realistic τ_{trans} is, therefore, estimated with the following equation, with d being the carrier displacement:

$$\tau_{\mathrm{trans}} = \frac{d}{\upsilon_{\mathrm{sat}}}. \tag{9}$$

In the worst case, where $d = 0.13\ \mu$m for a voltage change of 3 V, the time constant is calculated to be 1.63 ps. Although it is significantly larger than the ideal case, the small, picosecond scale of this term still shows the intrinsic advantage of devices working in depletion mode, as the operation speed is not limited by the slow diffusion of minority carriers.

The RC time constant, on the other hand, is determined by the series resistance and the barrier capacitance of the Schottky contact. These characteristic impedance values are dependent on the geometric dimension of the contact and are further influenced by nonideality factors such as skin effect, carrier inertia, and displacement current. In a realistic situation, one can define the dielectric relaxation frequency ω_d and the scattering frequency ω_s to count for the effect of the above-mentioned nonidealities [38]

$$\omega_d = \frac{\sigma}{\varepsilon_s \varepsilon_0} \tag{10}$$

$$\omega_s = \frac{e}{m^* \mu}. \tag{11}$$

In (10) and (11), σ is the conductivity, and μ represents the carrier mobility of the semiconductor. Assuming the Schottky contact and the semiconductor substrate are of circular shape of radii r and r', respectively, the bulk spread impedance and skin effect impedance are then defined as (μ_0 being the permeability of vacuum) [38]

$$Z_s = \frac{1}{4\sigma r}\left[\frac{1}{1 + j\omega/\omega_s} + j\omega/\omega_d\right]^{-1} \tag{12}$$

$$Z' = \frac{ln\left(r'/r\right)}{2\pi}\sqrt{\frac{j\omega\mu_0}{\sigma}}\left[\sqrt{\frac{1}{1 + j\omega/\omega_s} + j\omega/\omega_d}\,\right]^{-1}. \tag{13}$$

The barrier capacitance is calculated by

$$C = \frac{\pi r^2 \varepsilon_s \varepsilon_0}{D_{\text{dep}}} = \pi r^2 \sqrt{\frac{eN\varepsilon_s\varepsilon_0}{2\left(V_{bi} + V\right)}}. \tag{14}$$

The RC time constant can then be obtained by solving the following equations:

$$\text{Re}\left(Z_s\right) + \text{Re}\left(Z'\right) - \frac{1}{\omega C} = 0 \tag{15}$$

$$\tau_{RC} = \frac{2\pi}{\omega}. \tag{16}$$

In our structure, the surface area of the substrate on the groove region is $A = 14.2\ \mu\text{m} \times 3.3\ \mu\text{m}$. To the first order of approximation, we choose $r' = 3.86\ \mu$m in our calculation to represent a substrate of the same area. The RC time constant is plotted against the radius r in Fig. 11.

In Fig. 11, the RC time constant increases proportionally with the Schottky contact radius when skin effect, carrier inertia, and displacement current are not considered in the calculation. In real-world scenarios, however, those nonideality factors can have a significant influence on the characteristic impedance of the contact, and RC time constant is seen to deteriorate greatly from the ideal case when it is close to the plasmonic resonance frequency of GaAs. In our case, τ_{RC} is reasonably far from such resonance with the Schottky contact having the same area as the substrate and is calculated to be 1.2 ps.

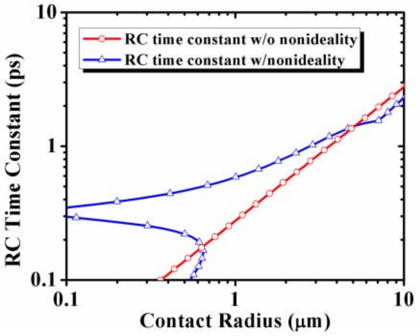

Fig. 11. RC time constant calculated both with and without the nonideality factors (skin effect, carrier inertia, and displacement current) as a function of the Schottky contact radius.

Taking both τ_{trans} and τ_{RC} back into (7), the maximum operating speed of our ADC is estimated to be 63.7 GS/s. It is noted that both the carrier transit time and the RC time constant can be further reduced by incorporating higher initial doping concentration of the n-GaAs region, which will feature smaller device dimensions as well as a thinner space-charge region.

VI. CONCLUSION

In this paper, we have designed and analyzed a terahertz beam steering structure by utilizing SSPP mode E-M propagation through the doubly-corrugated closed waveguide having subwavelength dimensions. The SSPP mode propagation is further enhanced by adding a thin layer of doped n-GaAs on the groove walls of the waveguide. The modulation to the free carrier concentration of GaAs causes the change in phase for the propagating terahertz wave, which, by combining two corrugated waveguides to construct an interferometer, can induce significant deflection of the output beam.

The beam bender can operate in either the enhancement mode or the depletion mode, depending on the nature of the free carrier density modulation. In the enhancement mode, free carriers are injected thermally, optically, or electronically into the GaAs layer. In the depletion mode, free carriers are extracted from the semiconductor via an external voltage across the Schottky contact. In both cases, the radiation angle of the output is effectively modulated. The visible nonlinear change of the diversion angle can be effectively corrected when differential controls are applied to the double arms of the MZI structure. The dielectric constant of the GaAs varies with its free carrier concentration as well as frequency. As a result, for both operating modes, different combinations of the two parameters can be used to optimize the design, making it highly adaptable to various applications.

In an effort to achieve higher operating speed for analog-to-digital conversion, we have utilized the SSPP beam bender in a spatial-resolved binary encoded sensor array with terahertz response time. With a differential voltage input asserted to both the arms of the MZI, a symmetric deflection angle change as large as ±20° is achieved with nearly perfect linearity. Due to the beam steering effect being realized with only two interferometric branches, the far-field radiation pattern is not suitable for coupling into independent detectors. As a result, detectors with carefully designed gains and saturation powers are used in order to readout multiple bits. By employing the beam deflector operating in depletion mode, a 3-bit ADC is realized with the speed of operation exceeding 60 GS/s. The maximum speed of the device is limited by the drifting carrier transit time across the space-charge region, as well as the parasitic *RC* constant of the Schottky contact. These time constants can be potentially minimized with a higher initial doping concentration of the n-GaAs that will further boost the operating BW of the proposed ADC design.

ACKNOWLEDGMENT

The authors would like to thank Dr. G. Pomrenke for encouraging them to develop terahertz DC-SSPP waveguide structures for terahertz signal processing circuits.

REFERENCES

[1] D. M. Mittleman, R. H. Jacobsen, and M. C. Nuss, "T-ray imaging," *IEEE J. Sel. Topics Quantum Electron.*, vol. 2, no. 3, pp. 679–692, Sep. 1996.

[2] P. H. Siegel, "Terahertz technology in biology and medicine," *IEEE Trans. Microw. Theory Techn.*, vol. 52, no. 10, pp. 2438–2447, Oct. 2004.

[3] M. Tonouchi, "Cutting-edge terahertz technology," *Nature Photon.*, vol. 1, no. 2, pp. 97–105, 2007.

[4] P. U. Jepsen, D. G. Cooke, and M. Koch, "Terahertz spectroscopy and imaging—Modern techniques and applications," *Laser Photon. Rev.*, vol. 5, no. 1, pp. 124–166, 2011.

[5] H.-T. Chen *et al.*, "Ultrafast optical switching of terahertz metamaterials fabricated on ErAs/GaAs nanoisland superlattices," *Opt. Lett.*, vol. 32, no. 12, pp. 1620–1622, Jun. 2007.

[6] Y.-M. Shin, L. R. Barnett, D. Gamzina, N. C. Luhmann, M. Field, and R. Borwick, "Terahertz vacuum electronic circuits fabricated by UV lithographic molding and deep reactive ion etching," *Appl. Phys. Lett.*, vol. 95, no. 18, pp. 181505-1–181505-3, 2009.

[7] K. Song and P. Mazumder, "Active terahertz spoof surface plasmon polariton switch comprising the perfect conductor metamaterial," *IEEE Trans. Electron Devices*, vol. 56, no. 11, pp. 2792–2799, Nov. 2009.

[8] K. Song and P. Mazumder, "Dynamic terahertz spoof surface plasmon–Polariton switch based on resonance and absorption," *IEEE Trans. Electron Devices*, vol. 58, no. 7, pp. 2172–2176, Jul. 2011.

[9] J. Dintinger, I. Robel, P. V. Kamat, C. Genet, and T. W. Ebbesen, "Terahertz all-optical molecule-plasmon modulation," *Adv. Mater.*, vol. 18, no. 13, pp. 1645–1648, 2006.

[10] J. G. Rivas, J. A. Sanchez-Gil, M. Kuttge, P. H. Bolivar, and H. Kurz, "Optically switchable mirrors for surface plasmon polaritons propagating on semiconductor surfaces," *Phys. Rev. B*, vol. 74, no. 24, p. 245324, 2006.

[11] V. Giannini, A. Berrier, S. A. Maier, J. A. Sanchez-Gil, and J. G. Rivas, "Scattering efficiency and near field enhancement of active semiconductor plasmonic antennas at terahertz frequencies," *Opt. Exp.*, vol. 18, no. 3, pp. 2797–2807, 2010.

[12] K. Wang and D. M. Mittleman, "Metal wires for terahertz wave guiding," *Nature*, vol. 432, pp. 376–379, Nov. 2004.

[13] J. B. Pendry, L. Martin-Moreno, and F. J. Garcia-Vidal, "Mimicking surface plasmons with structured surfaces," *Science*, vol. 305, pp. 847–848, Aug. 2004.

[14] C. R. Williams, S. R. Andrews, S. A. Maier, A. I. Fernández-Domínguez, L. Martín-Moreno, and F. J. García-Vidal, "Highly confined guiding of terahertz surface plasmon polaritons on structured metal surfaces," *Nature Photon.*, vol. 2, pp. 175–179, Feb. 2008.

[15] F. J. Garcia-Vidal, L. Martin-Moreno, T. W. Ebbesen, and L. Kuipers, "Light passing through subwavelength apertures," *Rev. Mod. Phys.*, vol. 82, no. 1, pp. 729–787, 2010.

[16] P. A. George, C. Manolatou, F. Rana, A. L. Bingham, and D. R. Grischkowsky, "Integrated waveguide-coupled terahertz microcavity resonators," *Appl. Phys. Lett.*, vol. 91, no. 19, p. 191122, 2007.

[17] R. Mendis, V. Astley, J. Liu, and D. M. Mittleman, "Terahertz microfluidic sensor based on a parallel-plate waveguide resonant cavity," *Appl. Phys. Lett.*, vol. 95, no. 17, p. 171113, 2009.

[18] Z. Xu, K. Song, and P. Mazumder, "Analysis of doubly corrugated spoof surface plasmon polariton (DC-SSPP) structure with sub-wavelength transmission at THz frequencies," *IEEE Trans. Terahertz Sci. Techonol.*, vol. 2, no. 3, pp. 345–354, May 2012.

[19] H.-T. Chen, W. J. Padilla, J. M. O. Zide, A. C. Gossard, A. J. Taylor, and R. D. Averitt, "Active terahertz metamaterial devices," *Nature*, vol. 44, pp. 597–600, Nov. 2006.

[20] K. F. McDonald, Z. L. Samson, M. I. Stockman, and N. I. Zheludev, "Ultrafast active plasmonics," *Nature Photon.*, vol. 3, pp. 55–58, Dec. 2009.

[21] J. Shu, C. Qiu, V. Astley, D. Nickel, D. M. Mittleman, and Q. Xu, "High-contrast terahertz modulator based on extraordinary transmission through a ring aperture," *Opt. Exp.*, vol. 19, no. 27, pp. 26666–26671, 2011.

[22] H.-T. Chen, W. J. Padilla, M. J. Cich, A. K. Azad, R. D. Averitt, and A. J. Taylor, "A metamaterial solid-state terahertz phase modulator," *Nature Photon.*, vol. 3, pp. 148–151, Feb. 2009.

[23] T. A. Ibrahim *et al.*, "Lightwave switching in semiconductor microring devices by free carrier injection," *J. Lightw. Technol.*, vol. 21, no. 12, pp. 2997–3003, Dec. 2003.

[24] Q. Xu, S. Manipatruni, B. Schmidt, J. Shakya, and M. Lipson, "12.5 Gbit/s carrier-injection-based silicon micro-ring silicon modulators," *Opt. Exp.*, vol. 15, no. 2, pp. 430–436, 2007.

[25] A. M. Gutierrez *et al.*, "Ring-assisted Mach–Zehnder interferometer silicon modulator for enhanced performance," *J. Lightw. Technol.*, vol. 30, no. 1, pp. 9–14, Jan. 1, 2012.

[26] Z. Xu and P. Mazumder, "Bio-sensing by Mach–Zehnder interferometer comprising doubly-corrugated spoofed surface plasmon polariton (DC-SSPP) waveguide," *IEEE Trans. Terahertz Sci. Techonol.*, vol. 2, no. 4, pp. 460–466, May 2012.

[27] *MATLAB*, Mathworks Inc., Natick, MA, USA.

[28] S. Adachi, *Optical Properties of Crystalline and Amorphous Semiconductors: Materials and Fundamental Principles*. Norwell, MA, USA: Kluwer, 1999.

[29] S. Adachi, *Optical Properties of Crystalline and Amorphous Semiconductors: Numerical Data and Graphical Information*. Norwell, MA, USA: Kluwer, 1999.

[30] *Ansoft HFSS*, Ansys Inc., Pittsburgh, PA, USA.

[31] M. Shur, *Introduction to Electronic Devices*. New York, NY, USA: Wiley, 1996.

[32] J. R. Waldrop, "Schottky-barrier height of ideal metal contacts to GaAs," *Appl. Phys. Lett.*, vol. 44, no. 10, pp. 1002–1004, 1984.

[33] H. F. Taylor, "An optical analog-to-digital converter—Design and analysis," *IEEE J. Quantum Electron.*, vol. 15, no. 4, pp. 210–216, Apr. 1979.

[34] M. Jarrahi, R. F. W. Pease, D. A. B. Miller, and T. H. Lee, "Optical spatial quantization for higher performance analog-to-digital conversion," *IEEE Trans. Microw. Theory Techn.*, vol. 56, no. 9, pp. 2143–2150, Sep. 2008.

[35] R. H. Walden, "Analog-to-digital converter survey and analysis," *IEEE J. Sel. Areas Commun.*, vol. 17, no. 4, pp. 539–550, Apr. 1999.

[36] A. Khilo *et al.*, "Photonic ADC: Overcoming the bottleneck of electronic jitter," *Opt. Exp.*, vol. 20, no. 4, pp. 4454–4469, 2012.

[37] A. V. D. Ziel, "Infrared detection and mixing in heavily doped Schottky-barrier diodes," *J. Appl. Phys.*, vol. 47, no. 5, pp. 2059–2068, May 1976.

[38] K. S. Champlin and G. Eisenstein, "Cutoff frequency of submillimeter Schottky-barrier diodes," *IEEE Trans. Microw. Theory Techn.*, vol. 26, no. 1, pp. 31–34, Jan. 1978.

Zhao Xu received the B.S. degree in electronics engineering from Tsinghua University, Beijing, China, and the M.S. degree in electrical engineering from the University of Michigan, Ann Arbor, MI, USA, in 2008, where he is currently pursuing the Ph.D. degree.

Pinaki Mazumder (F'99) received the Ph.D. degree from the University of Illinois at Urbana-Champaign, Champaign, IL, USA, in 1988.

He is currently a Professor with the Department of Electrical Engineering and Computer Science, University of Michigan, Ann Arbor, MI, USA.